CHEMISTRY

# A highly stable lithium metal anode enabled by Ag nanoparticle–embedded nitrogen-doped carbon macroporous fibers

**Yongjin Fang[1], Song Lin Zhang[1], Zhi-Peng Wu[1,2], Deyan Luan[1], Xiong Wen (David) Lou[1]***



**Lithium metal has been considered as an ideal anode candidate for future high energy density lithium batteries. Herein, we develop a three-dimensional (3D) hybrid host consisting of Ag nanoparticle–embedded nitrogen-doped carbon macroporous fibers (denoted as Ag@CMFs) with selective nucleation and targeted deposition of Li. The 3D macroporous framework can inhibit the formation of dendritic Li by capturing metallic Li in the matrix as well as reducing local current density, the lithiophilic nitrogen-doped carbons act as homogeneous nucleation sites owing to the small nucleation barrier, and the Ag nanoparticles improve the Li nucleation and growth behavior with the reversible solid solution–based alloying reaction. As a result, the Ag@CMF composite enables a dendrite-free Li plating/stripping behavior with high Coulombic efficiency for more than 500 cycles. When this anode is coupled with a commercial $LiFePO_4$ cathode, the assembled full cell manifests high rate capability and stable cycling life.**

## INTRODUCTION

Owing to the ultrahigh theoretical specific capacity (3861 mAh $g^{-1}$) and low redox potential (−3.04 V versus standard hydrogen electrode), metallic lithium has been regarded as one of the most promising anode materials for high-energy density rechargeable batteries (*1*–*6*). However, the uncontrollable growth of Li dendrites and collapse of the solid electrolyte interphase (SEI) layer lead to low Coulombic efficiency (CE) and deteriorated cycling performance, which largely restrict the practical application of the Li metal anode (LMA) (*7*–*13*). Considerable efforts have been made to regulate the Li plating/stripping behaviors for stable Li metal batteries, including developing functional electrolytes (*14*–*18*), constructing well-designed three-dimensional (3D) host structures (*19*–*24*), and using artificial protection layers (*25*–*30*). Despite much progress (*31*, *32*), it remains a challenge to explore LMA with stable cycling life over 500 cycles at practical current densities greater than 1 mA $cm^{-2}$.

From the classical diffusion model of Sand's equation (eq. S1) (*33*, *34*), the formation of Li dendrites is controlled by the main factors of the local current density, initial $Li^+$ ion concentration, and transport nature of $Li^+$ ions. A high current density induces the rapid consumption of $Li^+$ ions, which, in turn, results in serious concentration polarization due to the advection- and diffusion-limited ion migration in the bulk electrolyte (*35*, *36*). This issue further induces the growth of Li dendrites because of the enlarged ionic flux around the rapidly growing dendrite tips (*37*–*39*). In this regard, constructing 3D electronically conductive porous hosts for Li deposition is highly desired due to the largely decreased local current density (*40*–*42*). For example, 3D porous carbon nanofibers are reported as fascinating Li hosts with high areal capacity and long life span (*43*, *44*). However, the conventional 3D frameworks can hardly regulate the $Li^+$ ion concentration near the electrode/electrolyte interface due to the inferior absorbing ability for $Li^+$ ions. It is worth noting that some lithiophilic species with high $Li^+$ ion absorbing ability, such as polar functional groups, are capable of reducing the Li nucleation overpotential and facilitating uniform Li plating (*45*–*49*). For example, the heteroatom-doped carbons have shown good lithiophilicity to guide homogenous Li nucleation (*50*). Besides, it is proved that the formation of Li-based surface alloy films can offer a robust interface for lithium deposition due to the enhanced Li diffusion coefficients in the alloy composite, leading to ultralow nucleation overpotential (*51*, *52*). For example, from the Ag-Li binary phase diagram (Fig. 1A), a series of solid solutions can be formed at a wide range of Li atom%. With this property of high solubility in Li, Ag nanoparticles can react with Li to form solid-solution interfaces, which has shown reduced Li nucleation energy, thus assisting the inward-growth plating of Li while avoiding surface deposition (*53*–*56*). In contrast, the Cu-Li binary diagram has only one solid-solution zone at low Li atom% (fig. S1). During the lithiation-delithiation process, Li dendrites will grow on planar Cu (Fig. 1B), resulting in degradation of the CE. Although the above tactics have been proposed and proven effective in suppressing dendritic Li growth, a hybrid structure design with integrated multiple advantages (such as 3D macroporous structures, lithiophilic sites, and solid-solution interface) is rarely reported. In addition, the exact working principle and mechanism of the lithium nucleation sites and deposition behaviors on the hybrid host are far from clear.

To achieve viable and stable LMAs operated under high current densities, herein, we develop a facile strategy to construct a 3D macroporous framework consisting of Ag nanoparticle–embedded nitrogen-doped carbon macroporous fibers (denoted as Ag@CMFs) as a host for stable LMAs. The Li deposition properties can be effectively regulated with the Ag@CMF host because of the following multilevel advantages: (i) a 3D macroporous conductive structure with a large surface area to efficiently decrease the local current density, (ii) a stretchable and stable skeleton to buffer the compressive stress during long-term cycling, (iii) the macroporous structure to accommodate the rapid volume change during high current operation, (iv) lithiophilic nitrogen-doped carbon sites to homogenize Li deposition and guide the crystal nucleus distribution, and (v) reversible Ag-Li solid solution–based alloying reactions to effectively eliminate nucleation barriers. These structural and compositional merits endow a uniform and smooth Li plating on Ag@CMFs even at a high areal capacity

[1]School of Chemical and Biomedical Engineering, Nanyang Technological University, 62 Nanyang Drive, Singapore 637459, Singapore. [2]Green Catalysis Center, College of Chemistry, Zhengzhou University, Zhengzhou 450001, P.R. China.
*Corresponding author. Email: xwlou@ntu.edu.sg

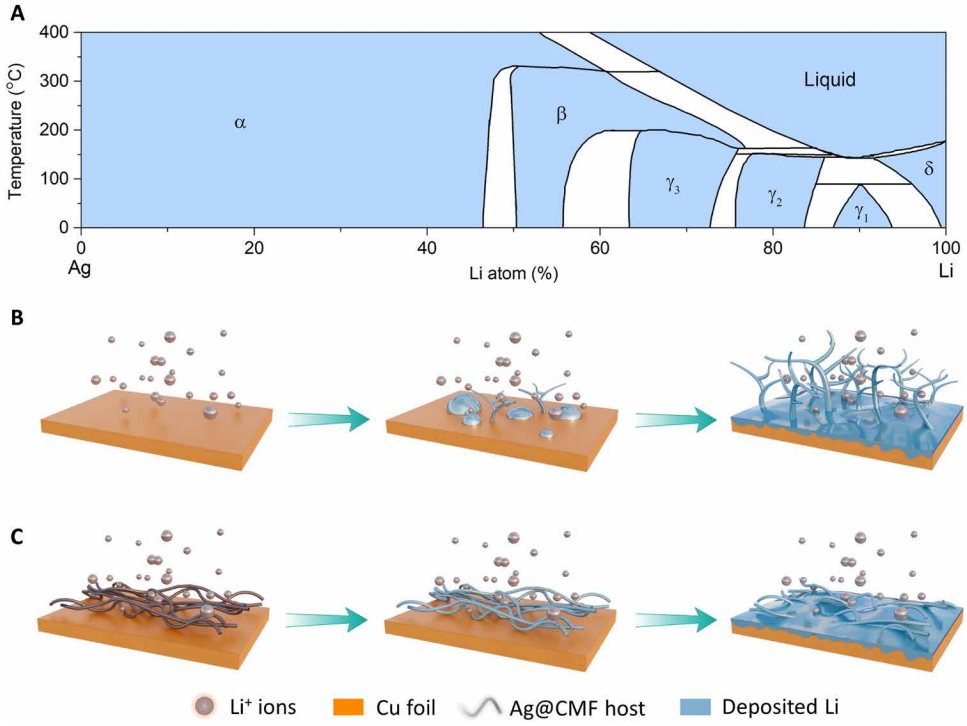


**Fig. 1. Ag-Li binary phase diagram and schematic illustration of Li deposition behaviors.** (**A**) Ag-Li binary phase diagram. (**B**) Lithium deposition on a planar copper foil. (**C**) Lithium deposition on Ag@CMFs.

deposition (Fig. 1C). As expected, the Ag@CMF composite enables a dendrite-free Li plating/stripping behavior with high CE for more than 500 cycles at different current densities. In addition, Ag@CMFs-Li symmetrical cells manifest superior rate capability and stable cycling performance at ultrahigh current densities over 10 mA $cm^{-2}$. Besides, when this anode is coupled with a $LiFePO_4$ (LFP) cathode, the Ag@CMFs-Li//LFP full cells also show high rate performance and long-term cycling life.

## RESULTS

### Fabrication and characterization of the Ag@CMF host

The Ag@CMFs are synthesized through an elaborate multistep templating strategy (Fig. 2A). $SiO_2$ nanospheres are adopted as the starting templates, and then Ag nanoparticles are deposited on the surface of the $SiO_2$ nanospheres through a redox reaction. Afterward, the $SiO_2$@Ag nanospheres are electrospun with polyacrylonitrile (PAN) to form the $SiO_2$@Ag@PAN nanofibers. After the following carbonization and etching treatments, the Ag@CMFs are obtained. As expected, the Ag@CMF host will significantly improve the comprehensive electrochemical properties of LMAs.

$SiO_2$ nanospheres with an average diameter of ~200 nm are synthesized through the Stöber method (Fig. 2, B and F, and fig. S2). Before Ag deposition, the $Sn^{2+}$-sensitized $SiO_2$ nanospheres are prepared (fig. S3). After deposition of Ag nanoparticles, the spherical structure is well maintained (Fig. 2C), and transmission electron microscopy (TEM) images further reveal the well-dispersed Ag nanoparticles on the surface of $SiO_2$ nanospheres with a size of 7 to 10 nm (Fig. 2G and fig. S4, A to C). Energy-dispersive x-ray (EDX) spectroscopy result (fig. S4D) confirms the presence of Ag element in the obtained product. Through the electrospinning process, the $SiO_2$@Ag nanospheres are compactly assembled with PAN, forming $SiO_2$@Ag@PAN fibers with a uniform diameter (Fig. 2D and fig. S5). TEM images indicate that the $SiO_2$@Ag nanospheres are well dispersed within the whole fiber (Fig. 2H). After the carbonization treatment in $N_2$, the resultant $SiO_2$@Ag@carbon composite retains the nanofiber morphology without apparent changes in appearance (Fig. 2, E and I, and fig. S6).

Then, the $SiO_2$ nanospheres in the $SiO_2$@Ag@carbon composite are completely etched by immersing the $SiO_2$@Ag@carbon in potassium hydroxide solution to generate the Ag@CMFs. The nanofiber structures are well preserved after the etching treatment (Fig. 3, A and B), and the enlarged observation reveals the rough surface of the nanofibers (Fig. 3C). TEM images show the hierarchical hollow structures with the spherical void spaces packed in a space-efficient arrangement (Fig. 3, D and E). The Ag nanoparticles are uniformly dispersed on the wall of the carbon sheath (Fig. 3, F and G, and fig. S7, A and B). Elemental mappings of a single Ag@CMF indicate the even distribution of Ag, C, and N elements in the hierarchical nanostructure (Fig. 3H and fig. S7C). The thermogravimetric analysis result discloses that the weight ratio of Ag nanoparticles in Ag@CMFs is determined to be about 30 weight % (wt %) (fig. S7D). In addition, the superior flexibility and decent mechanical properties of the obtained Ag@CMF paper can be visually verified through various mechanical deformations like bending, rolling, twisting, and even multiple folds (fig. S8). To show the essential function of the Ag nanoparticles for enhancing the Li deposition properties, a carbon macroporous fiber (denoted as CMF) host with a similar hierarchical hollow structure is prepared via a similar process but without the introduction of Ag nanoparticles (Fig. 3, I to L, and figs. S9 and S10).

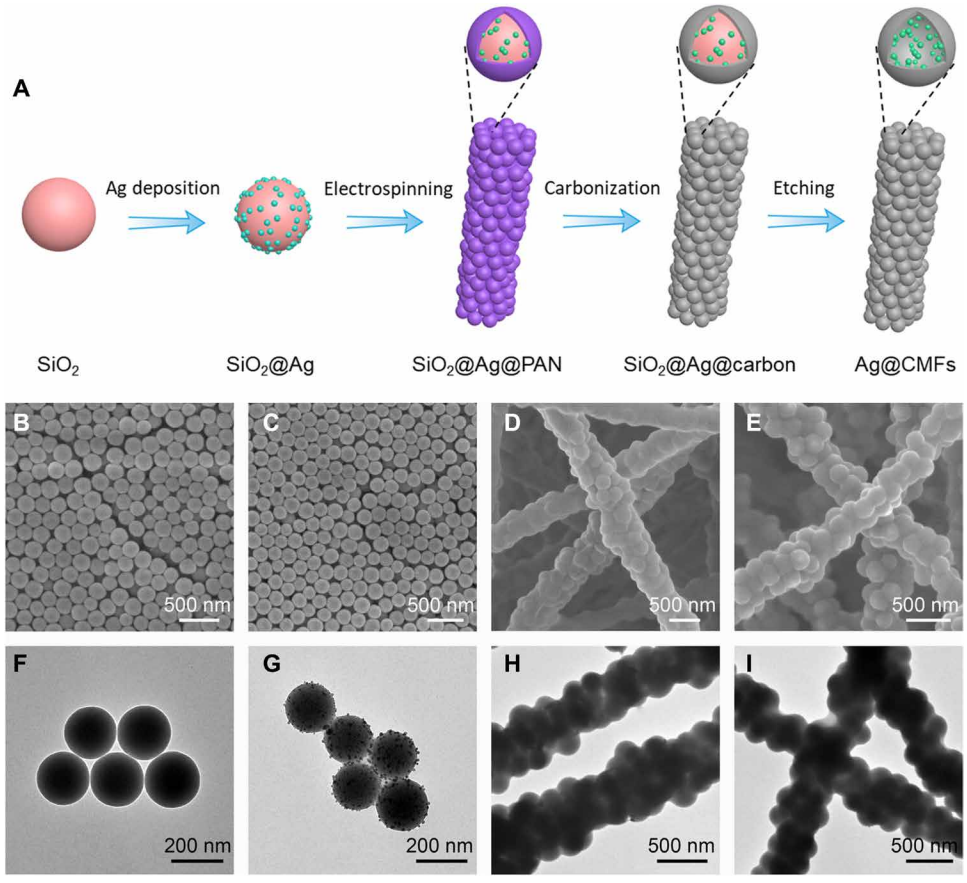


**Fig. 2. Fabrication strategy and characterization of the materials.** (**A**) Schematic illustration of the synthesis of Ag@CMFs. (**B** to **E**) Field-emission scanning electron microscopy (FESEM) images and (**F** to **I**) TEM images of the (B and F) $SiO_2$ nanospheres, (C and G) $SiO_2$@Ag nanospheres, (D and H) $SiO_2$@Ag@PAN fibers, and (E and I) $SiO_2$@Ag@carbon fibers.

The x-ray diffraction (XRD) pattern of the Ag@CMFs can be identified as metallic Ag phase (JCPDS card no. 89-3722), which is different from the amorphous character of the CMFs (Fig. 3M). The Ag@CMFs and CMFs show similar Raman spectra with typical D and G bands of carbon (Fig. 3N). Nitrogen adsorption/desorption isotherms reveal that the Ag@CMF composite has a mesoporous structure with a lower Brunauer-Emmett-Teller (BET) surface area (67.0 $m^2 g^{-1}$) compared to the CMFs (81.2 $m^2 g^{-1}$) (Fig. 3O). The surface chemical composition and element state of the Ag@CMFs are examined by x-ray photoelectron spectroscopy (XPS) analyses (fig. S11). Two strong peaks located at 368.1 and 374.1 eV are attributed to Ag $3d_{5/2}$ and Ag $3d_{3/2}$, respectively (Fig. 3P) (*54*). The three peaks in the high-resolution spectrum of C 1s are assigned to graphite-like $sp^2$ C, N-$sp^2$ C, and N-$sp^3$ C bonds (Fig. 3Q) (*57*). The four deconvoluted peaks located at 398.1, 399.7, 400.8, and 402.9 eV in the high-resolution N 1s spectrum show the presence of pyridinic N, pyrrolic N, quaternary N, and oxidized N species, respectively (Fig. 3R) (*58*). The lithiophilic nitrogen functional sites show larger binding energy (BE) and stronger adsorption ability for $Li^+$ ions, which will regulate the Li nucleation and growth properties (*50*).

## Li metal deposition behavior

The Li plating/stripping behavior on Ag@CMFs is investigated by a two-electrode cell configuration with 2032-coin cells, using Ag@CMFs as the working electrode and lithium foil as the counter/reference electrode. The typical discharge/charge voltage profiles of the Ag@CMF electrode at a current density of 1 mA $cm^{-2}$ are displayed in Fig. 4A. The nucleated Li starts to grow on Ag@CMFs when the voltage drops below 0 V. No Li dendrites are observed when the Li deposition capacity is as large as 2 mAh $cm^{-2}$ (Fig. 4B). TEM results reveal that the hollow structure becomes inconspicuous (fig. S12A), and nanoparticles are observed in the hollow spheres (fig. S12B), indicating that the Li is deposited mainly in the hollow interspace of porous carbon spheres (*43*, *51*). Besides, the XRD pattern and high-resolution TEM results confirm the formation of Li-Ag alloys (fig. S12, C and D). With further plating, obvious Li lumps instead of dendritic morphology are observed in the matrix when the areal capacity is higher than 5 mAh $cm^{-2}$ (Fig. 4C). When the deposition capacity of Li increases to a high value of 8 mAh $cm^{-2}$, pancake-like Li slices with a relatively smooth surface are observed without any visible dendritic Li (Fig. 4D), which is different from that observed on the planar Cu current collector with a large amount of Li filaments (fig. S13). Impressively, during the subsequent charging procedure, Li is stripped reversibly from the electrode accompanied by the gradual disappearance of the Li particles and the resurgence of the nanofiber structures (Fig. 4, E and F). After being charged to 1.5 V, Li is almost completely stripped from the electrode without any "dead Li" residue, and the 3D structure of the Ag@CMFs is well preserved (Fig. 4G), while the Ag nanoparticles

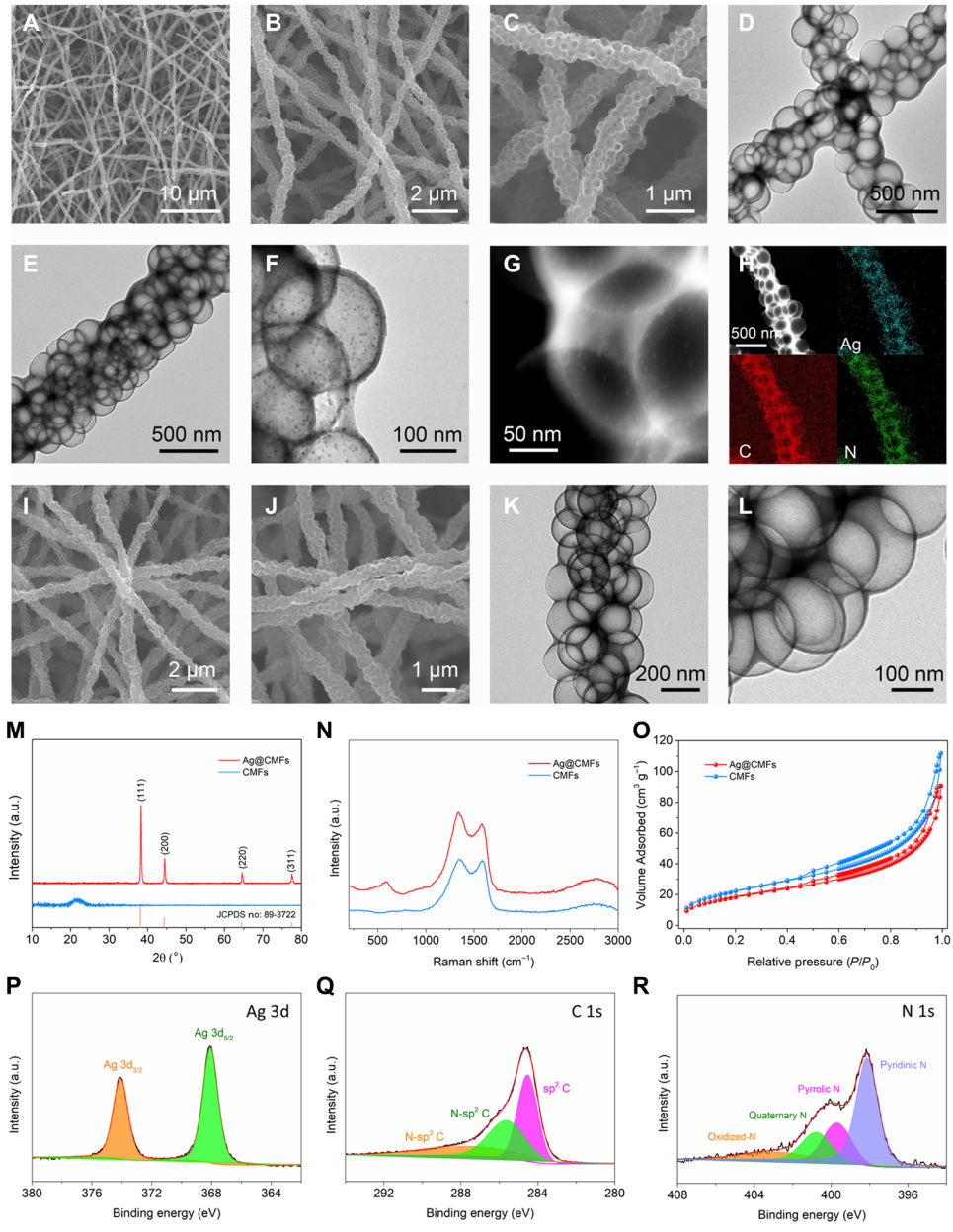


**Fig. 3. Characterization of the Ag@CMF and CMF materials.** (**A** to **C**, **I**, and **J**) FESEM images, (**D** to **F**, **K**, and **L**) TEM images, and (**G**) high-angle annular dark-field (HAADF)–scanning TEM (STEM) image of (A to G) Ag@CMFs and (I to L) CMFs. (**H**) Typical HAADF-STEM image and corresponding elemental mappings of Ag@CMFs. (**M**) XRD patterns, (**N**) Raman spectra, and (**O**) $N_2$ adsorption and desorption isotherms of Ag@CMFs and CMFs. a.u., arbitrary unit. (**P** to **R**) High-resolution XPS spectra of (P) Ag 3d, (Q) C 1s, and (R) N 1s of Ag@CMFs.

show some agglomeration (fig. S14). Besides, the CMFs exhibit a similar Li plating/stripping behavior compared to the Ag@CMFs (fig. S15). The outstanding regulation ability for Li plating/stripping of these Ag@CMFs could be attributed to the unique macroporous nanostructures and the synergistic effect of the lithiophilic nitrogen-doped carbon and Ag nanoparticles embedded. More specifically, the 3D macroporous framework with a high surface area endows significantly reduced local current density, leading to uniform metallic Li deposition without the formation of dendritic Li particles. The functional lithiophilic nitrogen-doped carbon sites can promote the Li nucleation and guide the crystal nucleus distribution. The distributed Ag nanoparticles facilitate ultralow nucleation barriers for guiding uniform nucleation and growth of Li in the macroporous 3D matrix. Besides, the appreciable flexibility and hollow structures can effectively accommodate the huge volume variation, thus enabling the release of compressive stress during repeated Li plating/stripping.

## Electrochemical performance

To evaluate the sustainability and reversibility of the Ag@CMF host for LMAs, the CE during galvanostatic plating/stripping processes is evaluated. The CE of typical coin cells cycled at different current densities is shown in Fig. 5A. The Ag@CMF electrode demonstrates

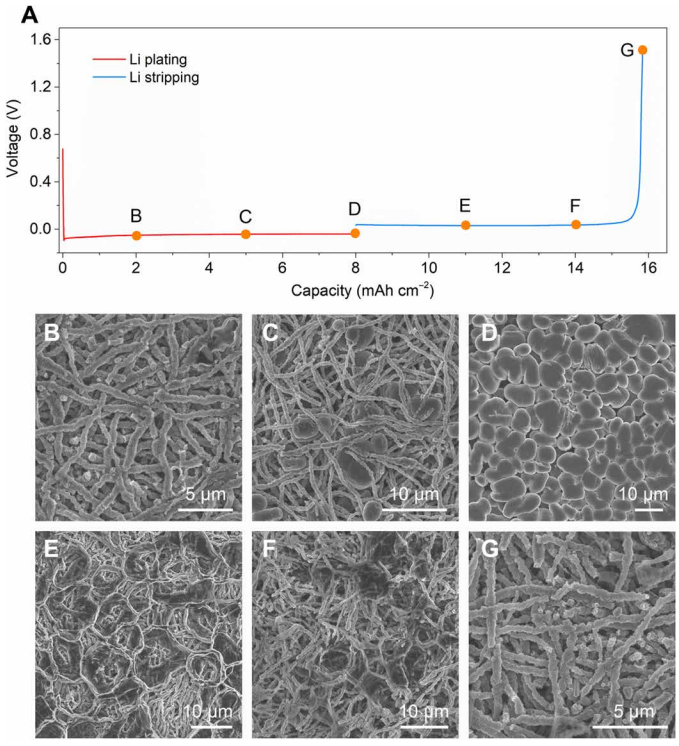


**Fig. 4. Li metal deposition behavior on Ag@CMFs.** (**A**) Electrochemical Li plating/stripping voltage profile of the Ag@CMF electrode at 1 mA cm$^{-2}$ for a capacity of 8 mAh cm$^{-2}$. (**B** to **G**) FESEM images of Ag@CMF electrodes after plating (B) 2 mAh cm$^{-2}$, (C) 5 mAh cm$^{-2}$, and (D) 8 mAh cm$^{-2}$ of Li metal into the Ag@CMFs; anodes after stripping (E) 3 mAh cm$^{-2}$, (F) 6 mAh cm$^{-2}$, and (G) 8 mAh cm$^{-2}$ (recharged to 1.5 V) from the Li anodes (8 mAh cm$^{-2}$) with the Ag@CMFs.

more stable cycling performance and longer cycling life compared to the CMFs and bare Cu foil (denoted as b-Cu). Specifically, the Ag@CMF electrode manifests high CE (>98%) for 800 cycles under a current density of 1 mA cm$^{-2}$. Even when a high current density of 5 mA cm$^{-2}$ is implemented, remarkable cycle life of 200 cycles can still be achieved. By contrast, the b-Cu electrode shows a much poorer cycle life of less than 120 cycles at different current densities. It should be noted that the CMF electrode exhibits much better cycling performance than the b-Cu, indicating the regulated Li plating/stripping behavior of the 3D macroporous nitrogen-doped carbon fibers. Besides, the Ag@CMF electrode demonstrates ultralow nucleation overpotentials and small polarization between discharge and charge curves at different current densities (fig. S16 and table S1). These results suggest that the decoration of Ag nanoparticles on 3D nitrogen-doped CMFs can effectively restrict the dead Li formation even at high current densities.

Symmetrical cells are then assembled to further evaluate the $Li^+$ ion transport capability of the Ag@CMFs. Before symmetrical cell assembly, 6 mAh cm$^{-2}$ of Li was plated onto the Ag@CMFs, CMFs, and planar Cu at a current density of 1 mA cm$^{-2}$ to form the Ag@CMFs-Li, CMFs-Li, and b-Cu-Li. The thickness of the Ag@CMFs-Li electrode is around 69 μm (fig. S17). The rate performance test of the Ag@CMFs-Li anode is conducted by cycling the symmetric cell at various current densities ranging from 0.5 to 30 mA cm$^{-2}$ with a fixed Li deposition capacity of 2 mAh cm$^{-2}$ (Fig. 5B). The Ag@CMFs-Li anode exhibits a small voltage polarization (<20 mV) when the current density reaches 5 mA cm$^{-2}$. Even at a high current density of 30 mA cm$^{-2}$, relatively small voltage hysteresis can still be achieved. Impressively, at a current density of 1 mA cm$^{-2}$ and deposition capacity of 1 mAh cm$^{-2}$, the Ag@CMFs-Li symmetric cell exhibits the lowest overpotential with remarkable cycling stability for 1000 hours (Fig. 5C). Even when further increasing the current density to ultrahigh values, the Ag@CMFs-Li anodes could still maintain stable cycling for 300 hours at 10 mA cm$^{-2}$ (Fig. 5D) and 250 cycles at 20 mA cm$^{-2}$ (fig. S18). The enlarged examinations (insets in Fig. 5, C and D) further confirm the stable and small electrochemical polarization during the long-term cycling. These results confirm that the Ag@CMF host can effectively improve the reversibility of Li plating/stripping.

To evaluate the potential application of the Ag@CMF electrode, full cells based on the Ag@CMFs-Li anode and a LFP cathode are assembled. The Ag@CMFs-Li//LFP full cell exhibits small polarization potential in both charge and discharge processes (fig. S19A). Notably, a decent capacity of 105 mAh g$^{-1}$ can be preserved even at a high current rate of 5 C (Fig. 5E and fig. S19B). Moreover, the Ag@CMFs-Li//LFP full cell also has remarkable cycling stability. Specifically, a capacity retention of 96% after 250 charge-discharge cycles at 1 C is achieved (Fig. 5F). The CE of the electrode maintains steadily around 100% during cycling. Comparatively, the capacity of the b-Cu-Li//LFP full cell fades markedly. Compared with the reported LFP-based full cells, the Ag@CMFs-Li//LFP cell manifests superior electrochemical performance in terms of both high rate capability and stable cycle life, indicating the feasibility of using the Ag@CMFs-Li anode for practical Li batteries.

## DISCUSSION

In general, the electrostatic interaction between the electronegative sites on the anode matrix and $Li^+$ ions in electrolyte plays a vital role in driving the $Li^+$ ion to the lithiophilic site for nucleation, and the nucleation behavior is greatly affected by the surface chemistry of the anode matrices (*50*, *52*). The lithiophilicity of the anode matrix can be quantitatively determined by evaluating the BE between lithium and matrix. A larger BE leads to a smaller Li nucleation barrier, thus resulting in a lower nucleation overpotential and smooth Li deposition (*23*, *50*, *54*).

To understand the Li nucleation behavior and reveal the lithiophilicity properties, density functional theory (DFT) calculation is used to determine the interaction between Li and the Ag@CMF matrix (Fig. 6A). The BEs between Li atom and different species are summarized in Fig. 6B. The adsorption of a Li atom is more sensitive to many nitrogen-doped carbons, which exhibit much stronger interactions compared to the Li atom on Cu (111) and Ag (111). This result suggests that the Li nucleation tends to take place on the nitrogen-doped carbon sites, which is consistent with reported results that lithiophilic heteroatom-doped carbon can effectively decrease the Li nucleation barrier and endow a homogenous Li deposition (*50*). To unveil the different lithiation properties of Cu and Ag, further simulation on the different lithiated $Ag_xLi_y$ and $Cu_xLi_y$ species with different configurations is conducted (Fig. 6C and fig. S20). The $Ag_xLi_y$ alloys tend to form the homogeneous atom dispersion with the highest BE, while the $Cu_xLi_y$ species are inclined to show the segregated atom dispersion with Li atoms occupying the surface sites. This observation is consistent with reported works that the Ag nanoseeds will dissolve into Li via the solid-solution reaction before the formation of the pure Li phase, thus providing a high Li atom diffusion

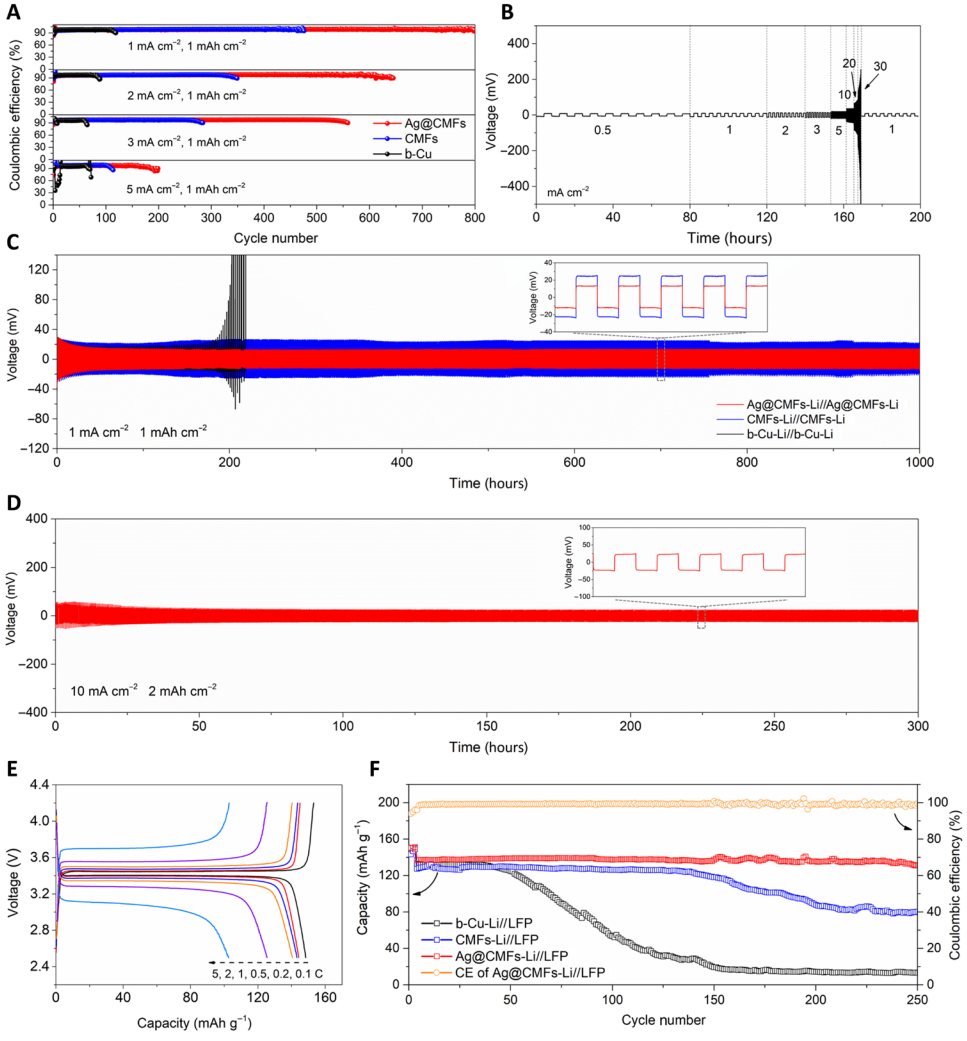


**Fig. 5. Electrochemical performance of different electrodes.** (**A**) CE of Li deposited on b-Cu, CMFs, and Ag@CMFs at different current densities for the same capacity of 1 mAh $cm^{-2}$. (**B**) Rate performance of Ag@CMFs-Li anode in an asymmetrical cell at various current densities with a fixed capacity of 2 mAh $cm^{-2}$. (**C**) Galvanostatic cycling voltage profiles of b-Cu-Li, CMFs-Li, and Ag@CMFs-Li anodes in symmetric coin cells at 1 mA $cm^{-2}$ with a capacity of 1 mAh $cm^{-2}$. (**D**) Ag@CMFs-Li anodes in symmetric coin cell at 10 mA $cm^{-2}$ with a capacity of 2 mAh $cm^{-2}$. (**E**) Galvanostatic charge/discharge curves of the Ag@CMFs-Li//LFP full cell at different current rates. (**F**) Cycling stability of the b-Cu-Li//LFP, CMFs-Li//LFP, and Ag@CMFs-Li//LFP full cells at 1 C (1 C = 170 mA $g^{-1}$).

coefficient and enabling stable cycling performance with high CE (*51*, *52*, *55*).

On the basis of the simulation results, we speculate the possible Li deposition process on the Ag@CMFs (Fig. 6D). The $Li^+$ ions in the electrolyte are driven to the lithiophilic nitrogen-doped carbon sites of the Ag@CMFs by the electric force. Once adsorbed on the nitrogen-doped carbon sites, the $Li^+$ ions are reduced to metallic Li because of charge transfer. When the lithiophilic sites are covered by few layers of Li atoms (fig. S21), the Li atoms tend to diffuse to the Ag nanoparticles and trigger the Li-Ag alloying reaction to form a solid-solution surface layer driven by the electrical energy and Li-Ag mixed reaction. The solid solution–based alloy phases grant the freshly generated Li atoms at the surface to easily diffuse into the formed alloy during further Li deposition hence eliminating the formation of Li dendrites.

In summary, we have designed Ag@CMFs as a 3D lithiophilic host for a robust and dendrite-free LMA. The 3D macroporous framework can mitigate the huge volume variation during Li plating/stripping processes and reduce the local current density. The lithiophilic nitrogen-doped carbon sites and functional Ag nanoparticles endow ultralow nucleation overpotential and small polarization. As a result, the nucleation and growth behavior of Li on the Ag@CMFs are effectively regulated. The Ag@CMF electrodes exhibit high CE (>98%) for more than 500 cycles at different current densities. In addition, the Ag@CMFs-Li symmetric cells show remarkable rate capability and stable cycling performance at ultrahigh current densities over 10 mA $cm^{-2}$. Encouragingly, the full cells made of the Ag@CMFs-Li anode and a LFP cathode exhibit superior rate capability and stable cycle life. These remarkable electrochemical properties endow the Ag@CMFs to be a highly promising host for LMAs. Furthermore, DFT simulations have been carried out to understand the regulated Li deposition behavior of the Ag@CMFs. The work may give a spark of inspiration for the design and construction of advanced functional 3D macroporous frameworks for LMAs in practical rechargeable batteries.

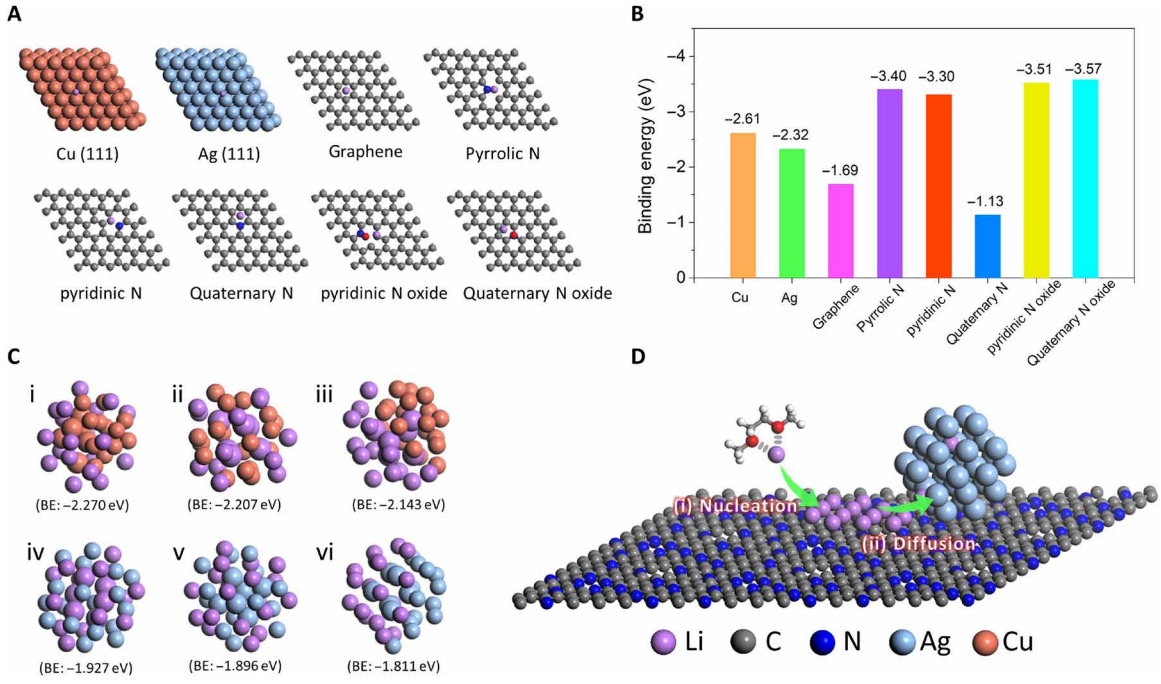


**Fig. 6. Modeling of the Li deposition on Ag@CMFs.** (**A**) Modeling of Ag, Cu, graphene, and nitrogen-doped carbons. (**B**) Summary of the calculated BE of Li atom with Cu, Ag, graphene, and nitrogen-doped carbons. (**C**) Different structures involving atom segregation and homogeneous dispersion configurations and the corresponding BEs of (i to iii) $Cu_{19}Li_{19}$ and (iv to vi) $Ag_{19}Li_{19}$ clusters. The higher BE represents the more stable configuration. (i) Atom segregation with Cu core, (ii) homogeneous dispersion, (iii) complete atom segregation, (iv) homogeneous dispersion, (v) atom segregation with Ag core, and (vi) complete atom segregation. (**D**) Schematic illustration of the Li deposition process on Ag@CMFs.

## MATERIALS AND METHODS

### Preparation of $SiO_2$ nanospheres

$SiO_2$ nanospheres were synthesized via the Stöber method (*59*). In a typical synthesis, 10 ml of deionized water, 70 ml of ethanol, and 5 ml of ammonia were mixed under stirring. Then, 3.5 ml of tetra-propyl orthosilicate was added to this solution and stirred at room temperature for 4 hours. The product was collected by centrifugation at 8000 rpm for 5 min and washed with ethanol several times.

### Preparation of $SiO_2$@Ag nanospheres

The $SiO_2$@Ag nanospheres were synthesized according to the previous work with minor modifications (*60*). First, 0.6 g of $SnCl_2{\cdot}2H_2O$ was dissolved into 50 ml of 0.1 M HCl, and then 0.5 g of the as-prepared $SiO_2$ nanospheres was added into the solution with sonication for 45 min. The $Sn^{2+}$-sensitized $SiO_2$ nanospheres were obtained by centrifugation at 8000 rpm for 5 min and washed with deionized water and ethanol several times. The as-prepared $Sn^{2+}$-sensitized $SiO_2$ nanospheres were dispersed into 10 ml of deionized water. Ammonical silver nitrate solution was prepared as follows: 0.5 g of silver nitrate was added into 40 ml of deionized water, followed by the addition of 0.2 ml of 0.1 M of NaOH under stirring, and then 2.5 ml of aqueous ammonia (6.6 wt %) was dropwise-added to the mixture to form the ammonical silver nitrate solution. The as-prepared $Sn^{2+}$-sensitized $SiO_2$ dispersion was added to the freshly prepared ammonical silver nitrate solution and stirred at room temperature for 1 hour. The precipitate was collected by centrifugation at 8000 rpm for 5 min and washed with deionized water and ethanol several times.

### Preparation of Ag@CMFs

First, 320 mg of as-prepared $SiO_2$@Ag nanospheres was ultrasonically dispersed in 2.5 ml of dimethylformamide (DMF) and mixed with 0.2 g of PAN under stirring at 60°C overnight. Then, the $SiO_2$@Ag@PAN nanofibers were electrospun on aluminum foil from the precursor solution. The solution was continuously fed at a rate of 1 ml $h^{-1}$, the distance between the collector and the stainless-steel needle was fixed at 12 cm, and a voltage of 17 kV was applied. The $SiO_2$@Ag@PAN nanofibers were first stabilized at 80°C for 2 hours in an oven and then annealed at 700°C for 3 hours in $N_2$. $SiO_2$ core was etched by immersing the nanofibers into 50 ml of 5.0 M KOH in a mixture solution of $H_2O$ and isopropanol alcohol (volume ratio of $H_2O$/isopropanol alcohol = 9:1) at 70°C for 48 hours in an oven. The Ag@CMFs were rinsed with deionized water several times and dried in a vacuum oven at 80°C for 24 hours before use.

### Preparation of CMFs

The CMFs were synthesized through a similar process using the $SiO_2$ nanospheres as template without the introduction of Ag nanoparticles. The experimental processes are the same as the synthesis of the Ag@CMFs.

### Materials characterizations

The morphology and structure of the samples were examined by FESEM (JEOL-6700) and TEM (JEOL, JEM-2010). The crystal phases of the samples were analyzed by XRD on a Bruker D2 Phaser X-ray Diffractometer with Ni filtered Cu Kα radiation (λ = 1.5406 Å) at a voltage of 30 kV and a current of 10 mA. The compositions of

the samples were analyzed by EDX spectroscope attached to the FESEM instrument. Elemental mapping images were recorded using an EDX spectroscope attached to TEM (JEOL, JEM-2100F). The chemical composition of the samples was analyzed by the XPS (PHI Quantum 2000) with the reference of C1s peak (284.6 eV). Thermogravimetric analysis was performed using a Shimadzu DTG-60 thermal analyzer under air flow (100 ml $min^{-1}$). $N_2$ adsorption-desorption isotherms were determined by Autosorb 6B at 77 K. Raman spectra were collected on a Renishaw Invia Reflex Raman microscope equipped with a 514-nm excitation laser.

### Electrochemical measurements

Electrochemical characterization was carried out using 2032-type coin cells. To evaluate the electrochemical deposition behavior and CE, the Ag@CMFs, CMFs, and planar Cu were used as the working electrodes. The areal mass loading of the Ag@CMF electrode is around 0.5 mg $cm^{-2}$. As LMAs based on ether-based electrolytes could frequently offer a higher CE compared to that of ester-based electrolytes because of the inhibition of the growth of lithium dendrites, 1 M lithium bis(trifluoromethanesulfonyl)imide in a mixture solution of 1,3-dioxolane and dimethoxyethane (1:1 v/v) with 2 wt % lithium nitrate was used as the electrolyte. Li foil was used as the counter/reference electrode. To form a stable SEI on the Ag@CMFs and CMFs, the batteries were first cycled between 0.01 and 1.5 V (versus $Li/Li^+$) at 0.1 mA $cm^{-2}$ for three cycles. The cycling performance was performed on a LAND cycler (Wuhan Kingnuo Electronic Co., China). Then, 6 mAh $cm^{-2}$ of Li was plated onto the Ag@CMFs, CMFs, or planar Cu at a current density of 1 mA $cm^{-2}$ to form the Ag@CMFs-Li, CMFs-Li, and b-Cu-Li. Symmetric cells were assembled using Ag@CMFs-Li, CMFs-Li, and b-Cu-Li electrodes to measure the long-term electrochemical behavior of Li plating/stripping. For the full cells, the cathode contains 80 wt % of commercial LFP powder, 10 wt % of Super-p, and 10 wt % of polyvinylidene difluoride binder using *N*-methyl-2-pyrrolidone as the solvent, and the well-mixed slurry was cast onto Al foil. The cathode with active LFP loading of ~4 mg $cm^{-2}$ was used in full cells, using 1.0 M $LiPF_6$ in ethylene carbonate and diethyl carbonate (v:v = 1:1) as the electrolyte to make the test conditions as close as possible to the real situation. For all the battery assembly, 50 μl of electrolyte was used for each cell. All the cells were assembled in a glove box with water/oxygen content lower than 0.5 parts per million and were tested at room temperature.

### Computational methods

Density functional calculations were performed using the $DMol^3$ package in the Materials Studio software. The exchange-correlation interaction was described by Perdew-Burke-Ernzerhof functional with a generalized gradient approximation. A double numerical basis set with polarization functions was applied. A $(3 \times 3 \times 1)$ *k*-point mesh was used to sample the Brillouin zone of the periodical graphene and nitrogen-doped graphene models. A 15 Å vacuum space along the *z* direction was used. All atoms were allowed to relax during Li adsorption. The adsorption energy of adsorbate was determined by $\Delta E_{ad} = E_{adsorbate/surface} - E_{adsorbate} - E_{surface}$, where $E_{adsorbate/surface}$, $E_{adsorbate}$, and $E_{surface}$ are the total energies of the adsorbate on the surface model, the adsorbate, and the surface model, respectively. Cluster models with 38 atoms reflecting different structures were used to calculate the BEs, which were calculated by $\Delta E_{BE} = (E_{MmNn} - mE_M - nE_N)/(m + n)$, where $E_{MmNn}$, $E_M$, and $E_N$ denote the total energies of $M_mN_n$ cluster, M atom, and N atom, respectively, and *m* and *n* are the numbers of atoms.

## SUPPLEMENTARY MATERIALS

Supplementary material for this article is available at http://advances.sciencemag.org/cgi/content/full/7/21/eabg3626/DC1

## REFERENCES AND NOTES


1. M. Armand, J. M. Tarascon, Building better batteries. *Nature* **451**, 652–657 (2008).
2. L. Li, S. Basu, Y. Wang, Z. Chen, P. Hundekar, B. Wang, J. Shi, Y. Shi, S. Narayanan, N. Koratkar, Self-heating-induced healing of lithium dendrites. *Science* **359**, 1513–1516 (2018).
3. M. J. Zachman, Z. Tu, S. Choudhury, L. A. Archer, L. F. Kourkoutis, Cryo-STEM mapping of solid-liquid interfaces and dendrites in lithium-metal batteries. *Nature* **560**, 345–349 (2018).
4. J. Liu, Z. Bao, Y. Cui, E. J. Dufek, J. B. Goodenough, P. Khalifah, Q. Li, B. Y. Liaw, P. Liu, A. Manthiram, Y. S. Meng, V. R. Subramanian, M. F. Toney, V. V. Viswanathan, M. S. Whittingham, J. Xiao, W. Xu, J. Yang, X.-Q. Yang, J.-G. Zhang, Pathways for practical high-energy long-cycling lithium metal batteries. *Nat. Energy* **4**, 180–186 (2019).
5. Y. Cao, M. Li, J. Lu, J. Liu, K. Amine, Bridging the academic and industrial metrics for next-generation practical batteries. *Nat. Nanotechnol.* **14**, 200–207 (2019).
6. J. Zheng, M. S. Kim, Z. Tu, S. Choudhury, T. Tang, L. A. Archer, Regulating electrodeposition morphology of lithium: Towards commercially relevant secondary Li metal batteries. *Chem. Soc. Rev.* **49**, 2701–2750 (2020).
7. P. Albertus, S. Babinec, S. Litzelman, A. Newman, Status and challenges in enabling the lithium metal electrode for high-energy and low-cost rechargeable batteries. *Nat. Energy* **3**, 16–21 (2018).
8. Y. Chen, Z. Wang, X. Li, X. Yao, C. Wang, Y. Li, W. Xue, D. Yu, S. Y. Kim, F. Yang, A. Kushima, G. Zhang, H. Huang, N. Wu, Y.-W. Mai, J. B. Goodenough, J. Li, Li metal deposition and stripping in a solid-state battery via Coble creep. *Nature* **578**, 251–255 (2020).
9. Y. Liu, Q. Liu, L. Xin, Y. Liu, F. Yang, E. A. Stach, J. Xie, Making Li-metal electrodes rechargeable by controlling the dendrite growth direction. *Nat. Energy* **2**, 17083 (2017).
10. X. Wang, G. Pawar, Y. Li, X. Ren, M. Zhang, B. Lu, A. Banerjee, P. Liu, E. J. Dufek, J.-G. Zhang, J. Xiao, J. Liu, Y. S. Meng, B. Liaw, Glassy Li metal anode for high-performance rechargeable Li batteries. *Nat. Mater.* **19**, 1339–1345 (2020).
11. Y. Liang, H. Dong, D. Aurbach, Y. Yao, Current status and future directions of multivalent metal-ion batteries. *Nat. Energy* **5**, 646–656 (2020).
12. J. Zheng, L. A. Archer, Controlling electrochemical growth of metallic zinc electrodes: Toward affordable rechargeable energy storage systems. *Sci. Adv.* **7**, eabe0219 (2021).
13. J. Zheng, T. Tang, Q. Zhao, X. Liu, Y. Deng, L. A. Archer, Physical orphaning versus chemical instability: Is dendritic electrodeposition of Li fatal? *ACS Energy Lett.* **4**, 1349–1355 (2019).
14. Y. Lu, Z. Tu, L. A. Archer, Stable lithium electrodeposition in liquid and nanoporous solid electrolytes. *Nat. Mater.* **13**, 961–969 (2014).
15. L. Xiao, Z. Zeng, X. Liu, Y. Fang, X. Jiang, Y. Shao, L. Zhuang, X. Ai, H. Yang, Y. Cao, J. Liu, Stable Li metal anode with "ion-solvent-coordinated" nonflammable electrolyte for safe Li metal batteries. *ACS Energy Lett.* **4**, 483–488 (2019).
16. X. Han, Y. Gong, K. K. Fu, X. He, G. T. Hitz, J. Dai, A. Pearse, B. Liu, H. Wang, G. Rubloff, Y. Mo, V. Thangadurai, E. D. Wachsman, L. Hu, Negating interfacial impedance in garnet-based solid-state Li metal batteries. *Nat. Mater.* **16**, 572–579 (2017).
17. X. Ren, P. Gao, L. Zou, S. Jiao, X. Cao, X. Zhang, H. Jia, M. H. Engelhard, B. E. Matthews, H. Wu, H. Lee, C. Niu, C. Wang, B. W. Arey, J. Xiao, J. Liu, J.-G. Zhang, W. Xu, Role of inner solvation sheath within salt-solvent complexes in tailoring electrode/electrolyte interphases for lithium metal batteries. *Proc. Natl. Acad. Sci. U.S.A.* **117**, 28603–28613 (2020).
18. S. H. Lee, J.-Y. Hwang, J. Ming, Z. Cao, H. A. Nguyen, H.-G. Jung, J. Kim, Y.-K. Sun, Toward the sustainable lithium metal batteries with a new electrolyte solvation chemistry. *Adv. Energy Mater.* **10**, 2000567 (2020).
19. X. Wang, W. Zeng, L. Hong, W. Xu, H. Yang, F. Wang, H. Duan, M. Tang, H. Jiang, Stress-driven lithium dendrite growth mechanism and dendrite mitigation by electroplating on soft substrates. *Nat. Energy* **3**, 227–235 (2018).
20. H. Wang, D. Lin, Y. Liu, Y. Li, Y. Cui, Ultrahigh-current density anodes with interconnected Li metal reservoir through overlithiation of mesoporous $AlF_3$ framework. *Sci. Adv.* **3**, e1701301 (2017).
21. S. Jin, Y. Jiang, H. Ji, Y. Yu, Advanced 3D current collectors for lithium-based batteries. *Adv. Mater.* **30**, 1802014 (2018).

22. D. Lin, J. Zhao, J. Sun, H. Yao, Y. Liu, K. Yan, Y. Cui, Three-dimensional stable lithium metal anode with nanoscale lithium islands embedded in ionically conductive solid matrix. *Proc. Natl. Acad. Sci. U.S.A.* **114**, 4613–4618 (2017).
23. W. Zhang, H. L. Zhuang, L. Fan, L. Gao, Y. Lu, A "cation-anion regulation" synergistic anode host for dendrite-free lithium metal batteries. *Sci. Adv.* **4**, eaar4410 (2018).
24. Y. Fang, Y. Zeng, Q. Jin, X. F. Lu, D. Luan, X. Zhang, X. W. Lou, Nitrogen-doped amorphous Zn-carbon multichannel fibers for stable lithium metal anodes. *Angew. Chem. Int. Ed.* **60**, 8515–8520 (2021).
25. J. Xie, J. Wang, H. R. Lee, K. Yan, Y. Li, F. Shi, W. Huang, A. Pei, G. Chen, R. Subbaraman, J. Christensen, Y. Cui, Engineering stable interfaces for three-dimensional lithium metal anodes. *Sci. Adv.* **4**, eaat5168 (2018).
26. H. Yuan, J. Nai, H. Tian, Z. Ju, W. Zhang, Y. Liu, X. Tao, X. W. Lou, An ultrastable lithium metal anode enabled by designed metal fluoride spansules. *Sci. Adv.* **6**, eaaz3112 (2020).
27. X. Cao, X. Ren, L. Zou, M. H. Engelhard, W. Huang, H. Wang, B. E. Matthews, H. Lee, C. Niu, B. W. Arey, Y. Cui, C. Wang, J. Xiao, J. Liu, W. Xu, J.-G. Zhang, Monolithic solid-electrolyte interphases formed in fluorinated orthoformate-based electrolytes minimize Li depletion and pulverization. *Nat. Energy* **4**, 796–805 (2019).
28. H. Yuan, J. Nai, Y. Fang, G. Lu, X. Tao, X. W. Lou, Double-shelled C@$MoS_2$ structures preloaded with sulfur: An additive reservoir for stable lithium metal anodes. *Angew. Chem. Int. Ed.* **59**, 15839–15843 (2020).
29. L. Wang, A. Menakath, F. Han, Y. Wang, P. Y. Zavalij, K. J. Gaskell, O. Borodin, D. Iuga, S. P. Brown, C. Wang, K. Xu, B. W. Eichhorn, Identifying the components of the solid-electrolyte interphase in Li-ion batteries. *Nat. Chem.* **11**, 789–796 (2019).
30. S. Liu, X. Ji, N. Piao, J. Chen, N. Eidson, J. Xu, P. Wang, L. Chen, J. Zhang, T. Deng, S. Hou, T. Jin, H. Wan, J. Li, J. Tu, C. Wang, An inorganic-rich solid electrolyte interphase for advanced lithium-metal batteries in carbonate electrolytes. *Angew. Chem. Int. Ed.* **60**, 3661–3671 (2021).
31. Q. Zhao, X. Liu, J. Zheng, Y. Deng, A. Warren, Q. Zhang, L. Archer, Designing electrolytes with polymerlike glass-forming properties and fast ion transport at low temperatures. *Proc. Natl. Acad. Sci. U.S.A.* **117**, 26053–26060 (2020).
32. S. Choudhury, Z. Tu, A. Nijamudheen, M. J. Zachman, S. Stalin, Y. Deng, Q. Zhao, D. Vu, L. F. Kourkoutis, J. L. Mendoza-Cortes, L. A. Archer, Stabilizing polymer electrolytes in high-voltage lithium batteries. *Nat. Commun.* **10**, 3091 (2019).
33. G. Li, Z. Liu, Q. Huang, Y. Gao, M. Regula, D. Wang, L.-Q. Chen, D. Wang, Stable metal battery anodes enabled by polyethylenimine sponge hosts by way of electrokinetic effects. *Nat. Energy* **3**, 1076–1083 (2018).
34. H. J. S. Sand, III. On the concentration at the electrodes in a solution, with special reference to the liberation of hydrogen by electrolysis of a mixture of copper sulphate and sulphuric acid. *Lond. Edinburgh Dublin Philos. Mag. J. Sci.* **1**, 45–79 (1901).
35. D. Lin, Y. Liu, Y. Cui, Reviving the lithium metal anode for high-energy batteries. *Nat. Nanotechnol.* **12**, 194–206 (2017).
36. M. Li, J. Lu, X. Ji, Y. Li, Y. Shao, Z. Chen, C. Zhong, K. Amine, Design strategies for nonaqueous multivalent-ion and monovalent-ion battery anodes. *Nat. Rev. Mater.* **5**, 276–294 (2020).
37. J. Xiao, How lithium dendrites form in liquid batteries. *Science* **366**, 426–427 (2019).
38. M. D. Tikekar, S. Choudhury, Z. Tu, L. A. Archer, Design principles for electrolytes and interfaces for stable lithium-metal batteries. *Nat. Energy* **1**, 16114 (2016).
39. C. Fang, J. Li, M. Zhang, Y. Zhang, F. Yang, J. Z. Lee, M.-H. Lee, J. Alvarado, M. A. Schroeder, Y. Yang, B. Lu, N. Williams, M. Ceja, L. Yang, M. Cai, J. Gu, K. Xu, X. Wang, Y. S. Meng, Quantifying inactive lithium in lithium metal batteries. *Nature* **572**, 511–515 (2019).
40. Y. Liu, D. Lin, Y. Jin, K. Liu, X. Tao, Q. Zhang, X. Zhang, Y. Cui, Transforming from planar to three-dimensional lithium with flowable interphase for solid lithium metal batteries. *Sci. Adv.* **3**, eaao0713 (2017).
41. N. Li, W. Wei, K. Xie, J. Tan, L. Zhang, X. Luo, K. Yuan, Q. Song, H. Li, C. Shen, E. M. Ryan, L. Liu, B. Wei, Suppressing dendritic lithium formation using porous media in lithium metal-based batteries. *Nano Lett.* **18**, 2067–2073 (2018).
42. D. Lin, Y. Liu, Z. Liang, H.-W. Lee, J. Sun, H. Wang, K. Yan, J. Xie, Y. Cui, Layered reduced graphene oxide with nanoscale interlayer gaps as a stable host for lithium metal anodes. *Nat. Nanotechnol.* **11**, 626–632 (2016).
43. L. Liu, Y.-X. Yin, J.-Y. Li, N.-W. Li, X.-X. Zeng, H. Ye, Y.-G. Guo, L.-J. Wan, Free-standing hollow carbon fibers as high-capacity containers for stable lithium metal anodes. *Joule* **1**, 563–575 (2017).
44. T.-T. Zuo, X.-W. Wu, C.-P. Yang, Y.-X. Yin, H. Ye, N.-W. Li, Y.-G. Guo, Graphitized carbon fibers as multifunctional 3D current collectors for high areal capacity Li anodes. *Adv. Mater.* **29**, 1700389 (2017).
45. R. Zhang, X.-R. Chen, X. Chen, X.-B. Cheng, X.-Q. Zhang, C. Yan, Q. Zhang, Lithiophilic sites in doped graphene guide uniform lithium nucleation for dendrite-free lithium metal anodes. *Angew. Chem. Int. Ed.* **56**, 7764–7768 (2017).
46. C. Niu, H. Pan, W. Xu, J. Xiao, J.-G. Zhang, L. Luo, C. Wang, D. Mei, J. Meng, X. Wang, Z. Liu, L. Mai, J. Liu, Self-smoothing anode for achieving high-energy lithium metal batteries under realistic conditions. *Nat. Nanotechnol.* **14**, 594–601 (2019).
47. G. Huang, J. Han, F. Zhang, Z. Wang, H. Kashani, K. Watanabe, M. Chen, Lithiophilic 3D nanoporous nitrogen-doped graphene for dendrite-free and ultrahigh-rate lithium-metal anodes. *Adv. Mater.* **31**, 1805334 (2019).
48. Y.-W. Song, P. Shi, B.-Q. Li, X. Chen, C.-X. Zhao, W.-J. Chen, X.-Q. Zhang, X. Chen, Q. Zhang, Covalent organic frameworks construct precise lithiophilic sites for uniform lithium deposition. *Matter* **4**, 253–264 (2021).
49. B.-Q. Li, X.-R. Chen, X. Chen, C.-X. Zhao, R. Zhang, X.-B. Cheng, Q. Zhang, Favorable lithium nucleation on lithiophilic framework porphyrin for dendrite-free lithium metal anodes. *Research* **2019**, 4608940 (2019).
50. X. Chen, X.-R. Chen, T.-Z. Hou, B.-Q. Li, X.-B. Cheng, R. Zhang, Q. Zhang, Lithiophilicity chemistry of heteroatom-doped carbon to guide uniform lithium nucleation in lithium metal anodes. *Sci. Adv.* **5**, eaau7728 (2019).
51. K. Yan, Z. Lu, H.-W. Lee, F. Xiong, P.-C. Hsu, Y. Li, J. Zhao, S. Chu, Y. Cui, Selective deposition and stable encapsulation of lithium through heterogeneous seeded growth. *Nat. Energy* **1**, 16010 (2016).
52. X. Liang, Q. Pang, I. R. Kochetkov, M. S. Sempere, H. Huang, X. Sun, L. F. Nazar, A facile surface chemistry route to a stabilized lithium metal anode. *Nat. Energy* **2**, 17119 (2017).
53. P. Xue, S. Liu, X. Shi, C. Sun, C. Lai, Y. Zhou, D. Sui, Y. Chen, J. Liang, A hierarchical silver-nanowire-graphene host enabling ultrahigh rates and superior long-term cycling of lithium-metal composite anodes. *Adv. Mater.* **30**, 1804165 (2018).
54. R. Zhang, X. Chen, X. Shen, X.-Q. Zhang, X.-R. Chen, X.-B. Cheng, C. Yan, C.-Z. Zhao, Q. Zhang, Coralloid carbon fiber-based composite lithium anode for robust lithium metal batteries. *Joule* **2**, 764–777 (2018).
55. S. Jin, Y. Ye, Y. Niu, Y. Xu, H. Jin, J. Wang, Z. Sun, A. Cao, X. Wu, Y. Luo, H. Ji, L.-J. Wan, Solid-solution-based metal alloy phase for highly reversible lithium metal anode. *J. Am. Chem. Soc.* **142**, 8818–8826 (2020).
56. Y.-G. Lee, S. Fujiki, C. Jung, N. Suzuki, N. Yashiro, R. Omoda, D.-S. Ko, T. Shiratsuchi, T. Sugimoto, S. Ryu, J. H. Ku, T. Watanabe, Y. Park, Y. Aihara, D. Im, I. T. Han, High-energy long-cycling all-solid-state lithium metal batteries enabled by silver-carbon composite anodes. *Nat. Energy* **5**, 299–308 (2020).
57. S. Wang, B. Y. Guan, X. W. Lou, Rationally designed hierarchical N-doped carbon@$NiCo_2O_4$ double-shelled nanoboxes for enhanced visible light $CO_2$ reduction. *Energy Environ. Sci.* **11**, 306–310 (2018).
58. Y. Fang, X.-Y. Yu, X. W. Lou, Bullet-like $Cu_9S_5$ hollow particles coated with nitrogen-doped carbon for sodium-ion batteries. *Angew. Chem. Int. Ed.* **58**, 7744–7748 (2019).
59. H. Zhang, Y. Liu, T. Chen, J. Zhang, J. Zhang, X. W. Lou, Unveiling the activity origin of electrocatalytic oxygen evolution over isolated Ni atoms supported on a N-doped carbon matrix. *Adv. Mater.* **31**, 1904548 (2019).
60. K.-Y. Pan, Y.-F. Liang, Y.-C. Pu, Y.-J. Hsu, J.-W. Yeh, H. C. Shih, Studies on the photocatalysis of core-shelled $SiO_2$-Ag nanospheres by controlled surface plasmon resonance under visible light. *Appl. Surf. Sci.* **311**, 399–404 (2014).
61. M. Zhu, G. Qian, Z. Hong, Z. Wang, X. Fan, M. Wang, Preparation and characterization of silica-silver core-shell structural submicrometer spheres. *J. Phys. Chem. Solid* **66**, 748–752 (2005).
62. G. Taillades, J. Sarradin, Silver: High performance anode for thin film lithium ion batteries. *J. Power Sources* **125**, 199–205 (2004).



**Acknowledgments**

**Funding:** X.W.L. acknowledges the funding support from the National Research Foundation (NRF) of Singapore via the NRF investigatorship (NRF-NRFI2016-04) and Ministry of Education of Singapore via the AcRF Tier-1 grant (RG3/20). **Author contributions:** Y.F. and X.W.L. conceived the idea. Y.F. carried out the materials synthesis. Y.F. and S.L.Z. carried out materials characterizations and analyzed the experimental data. Y.F. and Z.P.W. proposed the lithium deposition concept and carried out the theoretical calculation. Y.F., D.L., and X.W.L. discussed the results and cowrote the manuscript. All authors read and commented on the manuscript. **Competing interests:** The authors declare that they have no competing interests. **Data and materials availability:** All data needed to evaluate the conclusions in the paper are present in the paper and/or the Supplementary Materials. Additional data related to this paper may be requested from the authors.

Submitted 30 December 2020
Accepted 1 April 2021
Published 21 May 2021
10.1126/sciadv.abg3626

**Citation:** Y. Fang, S. L. Zhang, Z.-P. Wu, D. Luan, X. W. Lou, A highly stable lithium metal anode enabled by Ag nanoparticle–embedded nitrogen-doped carbon macroporous fibers. *Sci. Adv.* **7**, eabg3626 (2021).